Research Square

Preprints are preliminary reports that have not undergone peer review.
They should not be considered conclusive, used to inform clinical practice,
or referenced by the media as validated information.

Effect of MnO2 and MnO2-NCNO addition on structural and nonlinear optical properties of CoWO4 ceramics

marzieh nadafan (m_naddafan@yahoo.com)
Shahid Rajaee Teacher Training University https://orcid.org/0000-0002-0052-7975
Masoumeh Ghalkhani
Shahid Rajaee Teacher Training University
Esmail Sohouli
Shahid Rajaee Teacher Training University

Research Article

Keywords: CoWO4, MnO2, Carbon nano-onion, Nanocomposite, Optical properties, Third-order nonlinear

Posted Date: July 26th, 2021

DOI: https://doi.org/10.21203/rs.3.rs-738260/v1

License: This work is licensed under a Creative Commons Attribution 4.0 International License.
Read Full License

Effect of MnO2 and MnO2-NCNO addition on structural and nonlinear optical properties of $CoWO_4$ ceramics

Marzieh Nadafan[1,a], Masoumeh Ghalkhani[2, a], Esmail Sohouli[2]

1 Department of Physics, Faculty of Science, Shahid Rajaee Teacher Training University, Lavizan, P.O. Box 1678815811, Tehran, Iran.

2Electrochemical Sensors Research Laboratory, Department of Chemistry, Faculty of Science, Shahid Rajaee Teacher Training University, Lavizan, P.O. Box 1678815811, Tehran, Iran.

[a] Corresponding Author, alternative Electronic mail: m_naddafan@yahoo.com , m.nadafan@sru.ac.ir (M. Nadafan), ghalkhani@sru.ac.ir (M. Ghalkhani), Tel.: 098 21 36040234. Fax: 098 21 36040615. Mobile: 098 9125633281.

Effect of MnO_2 and MnO_2-NCNO addition on structural and nonlinear optical properties of $CoWO_4$ ceramics

Abstract

The nitrogen-doped carbon nano-onions (NCNOs) were prepared by annealing the ultra-dispersed aminated-nanodiamond solution under He gas at 1150 °C followed by calcination at 400°C. The nanostructures of $CoWO_4$, MnO_2, $CoWO_4$-MnO_2, and $CoWO_4$-MnO_2-NCNO were synthesized through the simple precipitation method under ultrasonication followed by calcination at 450°C. The morphology, structure, and optoelectronic properties of the samples were examined by scanning electron microscopy (SEM), X-ray diffraction (XRD), Fourier transform infrared (FTIR) spectroscopy and Z-scan method. The homogeneous distribution of the tiny aggregated plate-like and spongy particles throughout the nanocomposite created a highly porous nanostructure with a large surface area. The nonlinear absorption (NLA) coefficient and nonlinear refractive (NLR) index were of the order of $10^{-3}(cm/W)$ and $10^{-8}(cm^2/W)$, respectively. In different incident intensity of laser, all synthesized samples show TPA effect implying the positive sign of NLA coefficient. MnO_2 and NCNO structure have positive NLR index indicating the self-focusing optical nonlinearity. The self-defocusing effect and the negative sign of nonlinearity in the $CoWO_4$ nanoparticles, MnO_2-$CoWO_4$, and MnO_2-NCNO-$CoWO_4$ nanocomposites are vivid. The porous structure of $CoWO_4$ nanoparticles and trapping the light into $CoWO_4$ nanoparticles are the main reasons for nonlinearity of this nanoparticles. Porosity is also one of the most important reasons for the nonlinear optical responses of NCNO structure. The NLR index and NLA coefficient of MnO_2 decreased by increasing the incident intensity. Moreover, an increase in the incident intensity improved the

nonlinear responses in the rest of samples. The present nonlinear optical results of the synthesized samples can be applied in optical devices.

Keywords: $CoWO_4$, MnO_2, Carbon nano-onion, Nanocomposite, Optical properties, Third-order nonlinear

1. Introduction

Over the last decade, novel optical features have been discovered in nanoparticles that can not be observed in individual molecules and bulk metals [1]. According to several experimental investigations, the nanoparticle surfaces play critical roles in their linear and nonlinear optical behavior, including emission behavior and third-order optical nonlinearity [2]. Today, several photonic applications like optical power limiting, optical switching, optical modulating, and three-dimensional optical memory systems have been developed based on the nonlinear optical features of different materials. The nonlinear refractive (NLR) index of these structures is of crucial importance in the design of optical devices [3]. Incredible nonlinear optical features can be observed in several nanostructured materials, motivating the design and production of photonic systems [4, 5].

Remarkable physical characteristics have been observed by the extensive investigation of the optical nonlinearities in semiconductor nanomaterials. When the dimension of a semiconductor system reduces from bulk to nanoscale, the nonlinearity is enhanced as a result of the quantum size effect as well as other nanoparticle mesoscopic phenomena [6,7]. Furthermore, the properties of semiconductor materials could be tailored by changing their size, shape, and compositions to fit a diverse range of photonic and optoelectronic applications [7,8].

In this way, different types of materials were assessed to maximize the nonlinear optical properties. Due to its fascinating size and structure-dependent optical and electronic features, $CoWO_4$ has attracted much attention as a significant inorganic material [9]. $CoWO_4$ is a p-type semiconductor known for its amazing optical, electrical, and magnetic features. It can be applied in different areas including photovoltaic cells, electrochemical cells, pigment additive, gas sensor, and catalyst [10,11]. $CoWO_4$ nanoparticles have shown wide optical absorption band,

photothermal and photodynamic characteristics, and multimodal imaging abilities [12]. Moreover, this material has found applications in scintillation counters, lasers, and optical fibers. Some of its advantages like large mean refractive index and excellent chemical stability can be attributed to the tungstate as a self-activating phosphor. In this respect, the nonlinear optical properties of Er^{3+}-doped $ZnWO_4$ have been explored which indicated the applicability of MWO_4 (metal tungstates) laser for designing advanced photonic devices [13]. However, this property may be amplified with the incorporation or doping of other materials especially transition metal oxides.

Alternatively, since transition metal oxides including manganese oxides (MnO_2) are important components in solid-state batteries, they have been increasingly interested among researchers. As a significant group of dioxides, MnO_2 nanoparticles have over 14 polymorph forms. MnO_2 is classified as a transitional substance with versatile physical and chemical features including narrow bandgap, high optical constant, and ferroelectric characteristics [14]. Nano MnO_2 has shown outstanding capacitive properties when utilized as a supercapacitor. Its stable redox reaction, cost-effectiveness, and high theoretical capacitance (1370F/g) made it a suitable material for electrochemical capacitors [15]. The development of various MnO_2 nanocomposites containing conductive materials such as carbon-based or other transition metals compounds can enhance its electrical conductivity, which may also improve its nonlinear responses. The study of optical constants plays an important role in improving the optical features of MnO_2 thin film towards photovoltaic applications. To study the optical features of the MnO_2-containing composites, the optical nonlinearity of β-MnO_2 nano-thin films was determined which showed its suitability for nonlinear optoelectronic applications [16].

As an electrical double layer capacitor, carbon nano-onions (CNOs) store energy only through electrostatic interactions without any diffusion confinement, presenting the linear charge-discharge profile. They can supply high power density but very low energy density. CNOs possess exciting futures such as extended surface area and high mesoporosity [17]. Nonlinearity can be under the influence of high conductivity, large surface area, and porosity [18]. CNOs have been shown to offer various potential applications [19]. Optical properties of some CNO nanocomposites including the CNO/ZnO [20], CNO [21], CNO $C_{60}@C_{240}$ [19], and polyethyleneimine-poly(ethylene glycol)-CNO [22] have been studied but there is no report on the optical nonlinearity of pure CNO.

Therefore, various composites including CNO, MnO_2, and $CoWO_4$ constituents were generated for enhancing the nonlinearity of components. In the present communication, nitrogen-doped CNOs(NCNO), $CoWO_4$, and MnO_2 were prepared in the form of hybrid nanostructures to improve the nonlinear optical behavior.

2. Experimental

2.1. Reagents and Materials

The commercially available powder of the aminated-nanodiamond (AND, 4 nm ≤ crystal sizes ≤ 6 nm, purity more than 97 %) was purchased from Carbodeon μDiamond®Molto, Vantaa, Finland. All other utilized chemical and compounds were of analytical grade and were purchased from Merck, and used as received without further treatment.

2.2. Synthesis of NCNO

The ultra-dispersed AND solution was employed for preparation of NCNO. The procedure was according to a process developed by Kuznetsov with some modification [23]. The ultra-dispersed AND solution was annealed under He gas (1.1 MPa). The temperature was raised to 1150 °C and

let the reaction to be done for 60 min. Then, the temperature was slowly decreased to ambient condition during 60 min. After that, resulted product was annealed at 400 °C in an open air furnace to eliminate the amorphous carbon.

2.3. Synthesis of $CoWO_4$ Nanostructure

One liter of 0.4 M $Na_2WO_4.2H_2O$ aqueous solution was prepared by dissolving 131.9 mg of $Na_2WO_4.2H_2O$ salt in 1000 mL D.I. water, which was named as solution A. The 0.4 M Co (II) solution was prepared by dissolving $Co(NO_3)_2.6H_2O$ in D.I. water. Then, the solution A was slowly added dropwise into the solution B in ratio of 1:1 in room temperature under vigorous stirring. The following reaction was took place:

$$Co(NO_3)_2 + Na_2WO_4 \longrightarrow CoWO_4\,(s) + NaNO_3 \qquad (1)$$

After that, the precipitated product was thoroughly washed with D.I water and filtered. The precipitate was dried at 100 ^oC for 24 h. Finally, the dried product was grounded to a fine powder using an agate mortar which further calcinated at 400 ^oC for 4 h.

2.4. Synthesis of $CoWO_4$-MnO_2 and MnO_2 nanostructures

1.0 g of the prepared $CoWO_4$ was dispersed in 100 mL of D.I water and 2.4 g $Mn(Cl)_2$ was dissolved into it. The pH of the solution was adjusted to 10 by adding adequate amount of NaOH and then stirred during 2 h. Then, the solution was ultrasonicated for 20 min after that was dried at 150 ^oC. The MnO_2 nanoparticles were prepared in the same manner without addition of $CoWO_4$.

2.5. Synthesis of $CoWO_4$-MnO_2-NCNO

1.0 g of the prepared $CoWO_4$ was dispersed in 100 mL of D.I water and 2.4 g $Mn(Cl)_2$ was dissolved into it. After adjusting the solution pH to 10, it was stirred for 2 h. Then, 100 mg NCNO powder was dispersed in the solution with the aid of 2 h magnetic stirring and 20 min

ultrasonication. The obtained precipitate was dried at 60 ^{o}C. Finally, the dried product was grounded to a fine powder using an agate mortar and further calcinated at 400 ^{o}C for 4 h. Fig. 1 indicated the whole synthesized procedure of $CoWO_4$-MnO_2-NCNO nanostructure.

2.6. Material characterization

Fourier transform infrared (FTIR) spectra were obtained using a Bruker FTIR spectrometer (Tensor) applying KBr pellets (wavenumber: 500-4000 cm^{-1}). The crystallinity and phase identification of the synthesized materials were evaluated by X-ray diffraction (XRD) performed by a diffractometer (Philips PW-1730) with Cu K_α line (λ = 0.15406 nm). The visual images of the morphology of the synthesized nano-materials were provided using a scanning electron microscopy (SEM, Zeiss SIGMA VP).

3. Results and discussion

3.1. Characterization of synthesized nanostructures

The functional groups in nanostructures of synthesized (NCNO, MnO_2, $CoWO_4$, $CoWO_4$-MnO_2, and $CoWO_4$-MnO_2-NCNO) were identified using FTIR analysis as depicted in Fig.2. Two distinct peaks in the FT-IR spectrum of NCNO at 1200 and 3429cm^{-1} correspond to the C-N and O-H stretching vibrations, respectively, confirming the presence of carboxylic groups with successful nitrogen doping in the formulation of synthesized material [24]. The appearance of the broad peaks at 1630 and 3435cm^{-1} in the FTIR spectrum of the MnO_2 samples could be assigned to the stretching vibration of H-O-H and O-H due to H_2O adsorption by nano MnO_2. Moreover, other peaks at 624 and 528cm^{-1} correspond to the bending vibrations of O-Mn-O bonds in the octahedral structure (MnO_6) of the resulted MnO_2 [25]. Concerning $CoWO_4$, the bands at 618 and 827cm^{-1} originated from O-W-O and W-O-W vibrations, respectively. Also, the stretching vibration band of O-H and the bending vibration of H-O-H groups (due to H_2O absorption by the

nano $CoWO_4$) appeared at 3428 and 1633cm^{-1}, respectively [26]. The FTIR spectrum of the $CoWO_4$-MnO_2 exhibited four peaks. Two peaks at 633 and 531cm^{-1}, one at 827cm^{-1}, and a broad peak at 3438cm^{-1}, which were related to the bending vibration of O-Mn-O, the stretching vibrations of W-O, and stretching of the O-H bonds (in adsorbed H_2O molecules), respectively. All mentioned peaks confirmed the formation of the $CoWO_4$-MnO_2 composite. The presence of characteristic peaks of $CoWO_4$, MnO_2, and NCNO in the FTIR spectrum of synthesized $CoWO_4$-MnO_2-NCNO nanocomposite at 824, 537, 633, and 1200cm-^{1}, respectively, confirmed the attachment of NCNO to the $CoWO_4$-MnO_2 nanostructure.

The structural phase and crystallinity of the fabricated nanostructures were analyzed by XRD analyses as illustrated in Fig.3. The position of the diffractions peaks and corresponding crystal planes along with reference JCPDS file No. are presented in Table 1. NCNO (Fig.3c) showed a very weak and broad peak at $2\Theta\sim43^{\circ}$ originated from remained nanodiamond (ND) precursor utilized for the synthesis of NCNO. The peak that appeared at $2\Theta\sim23^{\circ}$ approved the successful conversion of the sp^3 hybridization of the ND structure to the sp^2 in graphitic carbon with a crystal plane of (002) [27-30]. The XRD pattern of $CoWO_4$-MnO_2-NCNO (Fig.3e) exhibited the characteristic peak of $CoWO_4$-MnO_2 along with NCNO indicating the successful combination of the nano $CoWO_4$, MnO_2, and NCNO to form the $CoWO_4$-MnO_2-NCNO nanocomposite.

The SEM image of synthesized NCNO powder showed a layered structure composed of agglomerated nanoparticles of graphitized carbon (Fig.4). While the agglomerated small plates were observed in the SEM image of MnO_2 powder, the $CoWO_4$ was composed of spongy agglomerated particles. Although both showed homogeneous morphology. The composite formation of $CoWO_4$ and MnO_2 led to the appearance of larger nanoparticles with higher porosity. The same morphology was observed for $CoWO_4$-MnO_2-NCNO as the $CoWO_4$-MnO_2,

indicating that the addition of NCNOs to the composite structure did not influence the structure of the product. Note that all synthesized materials showed homogeneous distribution of their components.

3.2. Z-scan measurements

Among the techniques used to analyze nonlinear optical features, the Z-scan measurement has been widely applied for the analysis of NLR indices and the nonlinear absorption (NLA) coefficients owing to its great sensitivity as well as simplified architecture [31]. The NLA coefficient and NLR index of MnO_2, $CoWO_4$, $CoWO_4$-MnO_2, NCNO, and $CoWO_4$-MnO_2-NCNO nanostructures were simultaneously measured using a Z-scan apparatus with a CW Nd:YAG laser operated at 532nm. The single-beam Z-scan technique was employed in open- and closed-aperture(CA) experiments. The experimental Z-scan setup is depicted in Fig.5.

A double-convex lens was utilized for focusing the beam on a 19mm spot, and a motorized translational stage was applied for moving samples along the z-axis. At the focal point, CWlaser showed the peak intensity of $I_0 = 2P_0/(\pi\omega_0^2)$. A beam splitter divided the laser beam into two beams. One of them was employed as the reference beam and collected in the photodetector to adjust the stability; while the other beam was utilized as a pump beam for measuring the nonlinear transmittance of the samples. A photodetector was also used for recording the intensity of the far-field transmitted beam which passed through the aperture. The waist of the laser beam at the focal plane, ω_0 and the Rayleigh length $z_r = \pi\omega_0^2/\lambda$ were the criteria of the Z-scan analysis

The light transmitting into the sample was collected with the open-aperture (OA) Z-scan, such that the intensity-based absorption and the highest transmission in the translation of the sample through the focal point can be characterized. On the other hand, it only collects the on-axis section of the divergent and diffracted beam that has an aperture on the z-axis in the far-field.

By transferring samples thorough the focal length, the recorded data were normalized to 1. The following equation was used to calculate the NLA coefficient in the open aperture configuration of Z-scan:

$$T_{norm}(z) = \sum \frac{[-q_0(z,0)]^m}{(m+1)^{3/2}} \quad (2)$$

$$q_0(z,t) = (\beta I_0 L_{eff}) / (1 + z^2 / z_0^2) \quad (3)$$

Where $T_{norm}(z)$ is the normalized power and m shows the order of the multi-photon process ($m=1$ for two-photon absorption (TPA), $m=2$ for three-photon absorption (3PA))[32]. Furthermore, L_{eff} is the effective thickness of quartz cell defined as $L_{eff} = (1-e^{-\alpha l})/\alpha$. α and l are the linear absorption coefficient and the sample length, respectively. α can be calculated by [32]:

$$\alpha = \frac{1}{l} \ln(-\frac{P_{in}}{P_{out}}) \quad (4)$$

Where P_{in} and P_{out} are the input and output power of the laser beam after passing through the sample, respectively.

The CA Z-scan data divided by the data of the OA Z-scan present the NLR, n_2, given that both Z-scans perform at the identical incident intensity. In the CA Z-scan configuration, the normalized data was put in the following equation to calculate the NLR index [31]:

$$T_{norm}(z) = 1 - \frac{4(z/z_0)\Delta\varphi_0}{((z/z_0)^2+9)((z/z_0)^2+1)} \quad (5)$$

Where $\Delta\varphi_0$ depends on n_2 according to the following equation [31]:

$$\Delta\varphi_0 = 2\pi n_2 I_0 L_{eff} / \lambda \quad (6)$$

Where λ is the wavelength of the incident laser beam. For calculation of the nonlinear absorption coefficients, β, Eq.(2) was used for fitting the normalized transmittance acquired from the OA Z-

scan setup. Fig. 6 shows the scattered data acquired from the OA Z-scan setup, with a solid line indicating the theoretically fitted experimental data using Eq. (2).

For determining the amount of n_2, ΔT (distance between peak and valley) could be calculated at various intensities using the graphs in the CA Z-scan setup. Then the amount of n_2 for the evaluated intensities was computed through Eqs. (5) and (6). To retrieve the NLR indices of the synthesized samples, the normalized transmittances were fitted to Eq.(5).

According to Sheik-Bahae et al., the signs of NLR index are positive (or negative) if there is a valley to peak (or a peak to valley) in the experimental data of CA Z-scan setup [33]. The positive and negative NLR indices refer to the self-focusing and self-defocusing effect of laser in the materials, respectively [33]. The CA Z-scan curves are shown in Fig.7.

3.2.1. Nonlinearity responses of MnO_2

According to Fig.6(a), the approximately symmetrical curves with a minimum value at z=0 indicate the positive value of β. This nonlinearity could be ascribed to the two-photon absorption. The normalized curves for the CA Z-scan of MnO_2 nanoparticles (at the concentration of 0.1g/L) are shown in Fig.7(a) for altered incident intensities for the aperture linear transmission of S=0.27. As a peak appears after the valley, the NLR index is positive [34]; implying the self-focusing optical nonlinearity of the material. The amount of n_2 and β are listed in Table 2. The NLR index and NLA coefficient decreased by increasing the incident intensity and input power.

Similar studies on MnO_2 nanoparticles have revealed the presence of important nonlinear aspects in lower incident intensities. For example, the magnitude and order of nonlinear response in this study are in line with the results of a study on MnO_2 nanoparticles using a CW laser beam with 532 nm wavelength [35]. The decrease of nonlinearity response by increasing the incident intensity was also confirmed [35].

3.2.2. Nonlinearity of $CoWO_4$

Fig.6(b) depicted the nonlinear responses of $CoWO_4$ nanoparticles. According to OA Z-scan data, the sign of NLA of $CoWO_4$ is positive due to the two-photon absorption process. In the CA Z-scan data, the curve in Fig.7(b) shows the peak-valley shape, implying a negative sign of nonlinearity in the $CoWO_4$ nanoparticles due to a self-defocusing effect, which can be assigned to the local variation in the refractive index with the temperature. An increase in incident intensity attenuated the nonlinear responses of $CoWO_4$ nanoparticles. All linear and nonlinear optical parameters are tabulated in Table 2. The porous structure of $CoWO_4$ nanoparticles and trapping the light into $CoWO_4$ nanoparticles are the main reasons for nonlinearity [36]. Furthermore, the presence of the double bond also led to nonlinear optical responses, although it is not very effective compared to porosity.

Similar results of nonlinearity of the tungstate family were reported earlier (such as $NiWO_4$). The order of n_2 and β are in good agreement with the nonlinear responses of $NiWO_4$ nanoparticles. Furthermore, in lower incident intensity, the NLA amount of $CoWO_4$ was higher than $NiWO_4$ [37]. At higher intensities, no difference was recognized between $CoWO_4$ and $NiWO_4$ nonlinearity responses.

3.2.3. Nonlinearity responses of NCNO

Nonlinear optical parameters of NCNO were investigated by OA and CA Z-scan techniques as presented in Figs.6(c) and 7(c). A dip in the transmittance curve at the focus position of OA Z-scan data of NCNO pointed to positive signs of NLA, β, and two-photon absorption process. Furthermore, the valley-peak configuration of CA of NCNO Z-scan data presented the positive sign of NLR index, n_2, and self-focusing optical nonlinearity of NCNO structure. According to

recorded nonlinearity data listed in Table 2, an increase in the incident intensity and input power incremented the NLR index and NLA coefficient.

Consequently, different parameters (including particle size, surface passivation, and nature of the employed organic moieties along with the electronic band structure) should be considered to take the NLO responses of these carbon-based nanomaterials into account [38]. Porosity is one of the most important reasons for the nonlinear optical responses of CNO [36]. Moreover, nonlinear scattering could be another factor for recorded nonlinearity responses, especially at higher intensities [38].

Previous investigations comparing the nonlinear optical responses of certain nanodiamonds and onion-like nano-carbons also reported similar observations in which the onion-like nano-carbons showed greater nonlinear optical responses and optical limiting due to having more sp^2 carbons [31]. The onion-like carbon nanoparticles were found to exhibit weaker nonlinear optical responses in comparison with the present findings, in which the corresponding NLA coefficients β was $3\sim30\times10^{-11}$ m/W[38,39].

3.2.4. Nonlinearity responses of $CoWO_4$-MnO_2

The NLA of $CoWO_4$-MnO_2 nanocomposite was evaluated by OA Z-scan curves in different incident intensities as depicted in Fig.6(d). According to the OA Z-scan setup, the positive sign of β is related to the valley in the focus position of the transmittance curve. The two-photon absorption effect can lead to a dip in the center of the transmittance curve versus the z-axis. On the other hand, in the CA Z-scan setup, the valley is followed by a peak (Fig.7(d)). Thus, the sign of the NLR index is negative and the self-defocusing effect was dominant. The NLR and NLA are calculated and listed in Table 2.

As mentioned, the porosity plays a decisive role in the nonlinear optical responses of $CoWO_4$-MnO_2 nanocomposite. The $CoWO_4$-MnO_2 nanoparticles are larger than the $CoWO_4$ and MnO_2 nanoparticles. These bigger particles can convey high irradiation energy to the environment, resulting in density inhomogeneities that can scatter the light [40]. The $CoWO_4$-MnO_2 nanoparticles also exhibited porous structure. The impact of porosity is greater than the size of $CoWO_4$-MnO_2 nanocomposite, so the $CoWO_4$-MnO_2 nanocomposite enhanced the nonlinear responses compared to its constituent components. Moreover, an increase in the incident intensity improved the nonlinear responses.

3.2.5. Nonlinearity of $CoWO_4$-MnO_2-NCNO

The OA curves of $CoWO_4$-MnO_2-NCNO nanocomposite showed a minimum at the focal point implying a rise in light absorption of the sample compared to the linear regime. The increase in the optical absorption of $CoWO_4$-MnO_2-NCNO nanocomposites relative to the linear regime can be assigned to the minimum in the normalized transmittance curve of the OA Z-scan. Fig. 6(e) shows the scattered signals from the OA Z-scan setup, where the solid line specifies the theoretically fitted curve of the experimental data using Eq.(2). The CA normalized transmittance curves for $CoWO_4$-MnO_2-NCNO nanocomposite are shown in Fig.7(e). As observable, the CA curves indicated a peak-to-valley configuration for different incident intensities on the $CoWO_4$-MnO_2-NCNO nanocomposite. This shape reached a negative sign, reflecting the self-defocusing properties of the NLR index, n_2 for $CoWO_4$-MnO_2-NCNO nanocomposite [31].

The solid curves in Fig.7(e) are the best theoretical fit for the experimental data. The calculated nonlinear refractive indices of $CoWO_4$-MnO_2-NCNO nanocomposite are also listed in Table 2. By increasing the incident intensity, the NLA and NLR grew. As previously mentioned, the

porous structure of $CoWO_4$-MnO_2-NCNO nanocomposite trapped the laser light and improved the nonlinearity.

4. Conclusion

$CoWO_4$, MnO_2, NCNO, $CoWO_4$-MnO_2, and $CoWO_4$-MnO_2-NCNO nanostructures were successfully synthesized in this study. Their morphology, structure, and optoelectronic properties were examined by SEM, XRD, FTIR, and Z-scan techniques. The homogeneous distribution of the tiny aggregated plate-like and spongy particles throughout the nanocomposite created a highly porous nanostructure with a large surface area. The NLR index of the samples was positive or negative originating from the self-focusing and self-defocusing effect, respectively. Furthermore, the NLA coefficients of all samples indicated an increment in the absorption by passing the samples through the focus point. The porous structure of samples affected the rise in nonlinear absorption and reflection of samples. The excellent nonlinear optical responses of synthesized samples suggest their great promises for application in photonic devices.

Acknowledgment

The authors wish to express their gratitude to the Shahid Rajaee Teacher Training University.

References

[1] Li X, Snetkov IL, Yakovlev A, *et al.* Fabrication and performance evaluation of novel transparent ceramics RE:Tb3Ga5O12 (RE = Pr, Tm, Dy) toward magneto-optical application. *J Adv Ceram* 2021, **10**: 271–278.

[2] Zhang Y, Ma M, Wang X, *et al*. Second-order optical nonlinearity of surface-capped CdS nanoparticles and effect of surface modification. *J Phys Chem Solids* 2003, **64**: 927-931.

[3] Jamshidi-Ghaleh K, Mansour N, Nonlinear refraction measurements of materials using the moiré deflectometry. *Opt Commun* 2004, **234**: 419-425.

[4] Pang C, Li R, Li Z, *et al.* A novel hierarchical nanostructure for enhanced optical nonlinearity based on scattering mechanism. *Nano Micro Small* 2020, **16**: 2003172.

[5] Jagannath G, Sayyed MI, Alhuthali AMS, Nanosecond nonlinear optical, optical limiting and gamma radiation shielding attributes of Eu^{3+} ions doped heavy metal borate glasses. *Ceram Int* 2021, **47**: 14330-14340.

[6] Mahdy MA, Mahmoud EA, Mahdy IA, Linear and nonlinear optical response dependency on the crystallite *size* of CdTe and its structural properties. *Surf Interfaces* 2021, **23**: 100974.

[7] Tuniz A, Nanoscale nonlinear plasmonics in photonic waveguides and circuits. *Riv Nuovo Cim* 2021, **44**: 193-249.

[8] Sharaf ER, Yahia IS, Mohammed MI, *et al.* High refractive index and third-order nonlinear optical susceptibility of nanostructured ZnSe/FTO thin films: Towards smart multifunctional optoelectronic materials. *Physica B Condens Matter* 2021, **602**: 412595.

[9] Xiao EC, Liu M, Ren Q, *et al.* Phonon characteristics and dielectric properties of a phase pure CoWO4 ceramic. *Ceram Int* 2020, **46**: 15705-15708.

[10] Deng J, Chang L, Wang P, *et al.* Preparation and magnetic properties of $CoWO_4$ nanocrystals. *Cryst Res Technol* 2012, **47**: 1004-1007.

[11] Siqueira KP, Dias A, Incipient crystallization of transition-metal tungstates under microwaves probed by Raman scattering and transmission electron microscopy. *J Nanoparticle Res* 2011, **13**: 5927-5933.

[12] Liu H, Yang Q, Guo W, *et al.* $CoWO_4$-x-based nanoplatform for multimode imaging and enhanced photothermal/photodynamic therapy. *Chem Eng J* 2020, **385**: 123979.

[13] Rahulan KM, Flower AL, Padmanathan N, *et al.* Luminescence and nonlinear optical properties of Er^{3+}-doped $ZnWO_4$ nanostructures. *J Photochem Photobiol A: Chem* 2020, **386**: 112128.

[14] Zhao C, Wu Y, Liang H, *et al.* N-doped graphene and TiO2 supported manganese and cerium oxides on low-temperature selective catalytic reduction of NOx with NH3. *J Adv Ceram* 2018, **7**: 197–206.

[15] Luo X, Yang J, Yan D, *et al.* MnO_2-decorated 3D porous carbon skeleton derived from mollusc shell for high-performance supercapacitor. *J Alloys Compd* 2017, **723**: 505-511.

[16] Makhlouf M, Preparation and optical characterization of β-MnO_2 nano thin films for application in heterojunction photodiodes. *Sens Actuators A: Phys* 2018, **279**: 145-156.

[17] Pandolfo AG, Hollenkamp AF, Carbon properties and their role in supercapacitors. *J Power Sources* 2006, **157**: 11-27.

[18] Gadhwal R, Devi A, A review on the development of optical limiters from homogeneous to reflective 1-D photonic crystal structures. *Opt Laser Technol* 2021, **141**: 107144.

[19] Voityuk AA, Solà M, Photoinduced charge separation in the carbon nano-onion C60@ C240. *J Phys Chem A* 2016, **120**: 5798-5804.

[20] Bobrowska DM, Castro E, Echegoyen L, *et al.* Carbon nano-onion and zinc oxide composites as an electron transport layer in inverted organic solar cells. *Chem Nano Mat* 2020, **6**: 248-257.

[21] Panda A, Arumugasamy SK, Lee J, *et al.* Chemical-free sustainable carbon nano-onion as a dual-mode sensor platform for noxious volatile organic compounds. *Appl Surf Sci* 2021, **537**: 147872.

[22] Sun W, Zhang X, Jia HR, *et al.* Water-Dispersible Candle Soot–Derived Carbon Nano-Onion Clusters for Imaging-Guided Photothermal Cancer Therapy. *Nano Micro Small* 2019, **15**: 1804575.

[23] Kuznetsov VL, Butenko YV. Synthesis, Properties and Applications of Ultrananocrystalline Diamond. In *Nanodiamond Graphitization and Properties of Onion-Like Carbon.* Gruen DM, Shenderova OA, Vul' AY, Eds. Dordrecht: Springer, 2005: 199-216.

[24] Sikeyi LL, Ntuli TD, Mongwe TH, *et al.* Microwave assisted synthesis of nitrogen doped and oxygen functionalized carbon nano onions supported palladium nanoparticles as hybrid anodic electrocatalysts for direct alkaline ethanol fuel cells. *Int J Hydrog Energy* 2021, **46**: 10862-10875.

[25] Ghosh D, Bhandari S, Khastgir D, Synthesis of MnO_2 nanoparticles and their effective utilization as UV protectors for outdoor high voltage polymeric insulators used in power transmission lines. *Phys Chem Chem Phys* 2016, **18**: 32876-32890.

[26] Sagadevan S, Podder J, Das I, Synthesis and characterization of $CoWO_4$ nanoparticles via chemical precipitation technique. *J Mater Sci: Mater Electron* 2016, **27**: 9885-9890.

[27] Tomita S, Burian A, Dore JC, *et al.* Diamond nanoparticles to carbon onions transformation: X-ray diffraction studies. *Carbon* 2002, **40**: 1469-1474.

[28] Tomita S, Sakurai T, Ohta H, *et al.* Structure and electronic properties of carbon onions. *J Chem Phys* 2001, **114**: 7477-7482.

[29] Dhand V, Prasad JS, Rao MV, *et al.* Flame synthesis of carbon nano onions using liquefied petroleum gas without catalyst. *Mater Sci Eng C* 2013, **33**: 758-762.

[30] Teraoka EYM, Broaddus DH, Kita T, *et al.* Self-phase modulation at visible wavelengths in nonlinear ZnO channel waveguides. *Appl Phys Lett* 2010, **97**: 071105.

[31] Sheik-Bahae M, Said AA, Van Stryland EW, High-sensitivity, single-beam $n2$ measurements. *Opt Lett* 1989, **14**: 955-957.

[32] Majles Ara MH, Dehghani Z, Nadafan M, The effect of external applied fields on the third order nonlinear susceptibility and two-photon absorption cross-section of E5CN7@Fe3O4-CNT. *Opt Laser Technol* 2019, **119**: 105653.

[33] Sabbaghan M, Nadafan M, Lamei HR, Cu-doped ZnO synthesis by ionothermal method: Morphology and optical properties. *Opt Mater* 2021, **111**: 110679.

[34] Mousavi M, Nadafan M, Tabatabai Yazi Sh, Third-order optical nonlinear properties of Co-doped V2O5 nanoparticles. *Optik* 2021, **226**: 165925.

[35] Naderi H, Majles Ara MH, Zebarjadan H, *et al.* Nonlinear response of nano-particles birnessite-type Manganese oxide (γ-MnO_2). *Optik* 2013, **124**: 1560-1563.

[36] Nadafan M, Sabbaghan M, Sofalgar P, *et al.* Comparative study of the third-order nonlinear optical properties of ZnO/Fe3O4nanocomposites synthesized with or without Ionic Liquid. *Opt Laser Technol* 2020, **131**: 106435.

[37] Mani Rahulan K, Phebe Kokila I, Angeline Little Flower N, *et al.* Structural and third order nonlinear optical properties of Gd doped $NiWO_4$ nanostructures. *Opt Mater* 2018, **77**: 148-153.

[38] Papagiannouli I, Bourlinos AB, Bakandritsos A, *et al.* Nonlinear Optical Properties of Colloidal Carbon Nanoparticles: Nanodiamonds and Carbon Dots. *RCS Adv* 2014, **76**: 40152-40160.

[39] Koudoumas E, Kokkinaki O, Konstantaki M, *et al.* Onion-like carbon and diamond nanoparticles for optical limiting. *Chem Phys Lett* 2002, **357**: 336-340.

[40] Kislyakov IM, Yelleswarapu CS, Nonlinear scattering studies of carbon black suspensions using photoacoustic Z-scan technique. *Appl Phys Lett* 2013, **103**: 151104.

Table 1. The good agreement between XRD patterns of $CoWO_4$-MnO_2 and $CoWO_4$-MnO_2-NCNO

Sample	Peak position, 2Θ (degree)	Crystal planes	JCPDS file No.
NCNO	23	(002)	*Graphitization* of diamond *crystal [29]*
MnO_2	18.1, 27.8, 35.9, 41.9, 45.7	(200), (310), (211), (301), (411)	MnO_2: 44-0141
$CoWO_4$	18.99, 23.81, 24.65, 30.63, 37.8, 41.37, 44.33, 45.79, 54.04, 61.75	(100), (011), (110), (111), (002), (121), (112), (211), (221), (113)	$CoWO_4$: 15-0867
$CoWO_4$-MnO_2	17.65, 23.41, 24.7, 30.63, 37.9, 44.33, 49.7, 54.7, 62.9	-	-
$CoWO_4$-MnO_2-NCNO	18.9, 21.86, 24.65, 30.63, 37.1, 41.12, 44.33, 49.1, 53.2, 54.6	-	-

Table 2 Nonlinear optical properties of MnO_2, $CoWO_4$, NCNOs, $CoWO_4$-MnO_2 and $CoWO_4$-MnO_2-NCNO nanostructures in different power of laser.

Sample (x)	$P_0(mW)$	$\alpha(cm^{-1})$	$L_{eff}(mm)$	$\omega_0(\mu m)$	ΔT_{P-V}	$n_2\times10^{-8}$ $\left(cm^2/W\right)$	$\beta\times10^{-3}$ (cm/W)
MnO_2	20	0.33	0.983	35	0.84	8.582	9.401
	30	0.36	0.982	36	0.53	8.280	6.444
	40	0.39	0.981	38	0.43	5.624	0.654
	50	0.59	0.971	42	0.3	3.873	0.371
$CoWO_4$	20	0.92	0.955	35	0.10	2.278	0.085
	30	0.67	0.967	36	0.16	2.540	0.099
	40	0.67	0.967	38	0.20	2.653	0.116
	50	0.91	0.956	42	0.28	3.672	0.131
NCNO	20	0.59	0.971	35	0.32	7.196	0.504
	30	0.39	0.981	36	0.5	7.853	0.587
	40	0.33	0.984	38	0.61	7.981	1.141
	50	0.35	0.982	42	0.63	8.065	2.727
$MnO_2/CoWO_4$	20	1.57	0.925	35	0.14	3.304	0.176
	30	1.32	0.936	36	0.22	3.618	0.184
	40	1.05	0.949	38	0.30	4.068	0.186
	50	1.11	0.946	42	0.44	5.847	0.232
$MnO_2/CoWO_4$/NCNO	20	0.56	0.972	35	0.27	6.064	0.252
	30	0.59	0.971	36	0.40	6.347	0.257
	40	0.83	0.959	38	0.48	6.439	0.284
	50	0.50	0.975	42	0.50	6.449	0.369

Figure Captions:

Fig. 1. Experimental procedure of synthesized $CoWO_4$-MnO_2-NCNO nanocomposites.

Fig. 2. FTIR spectra of the synthesized nanomaterials.

Fig. 3. XRD patterns of the (a) MnO_2, (b) $CoWO_4$, (c) NCNO, (d) $CoWO_4$-MnO_2, and (e) $CoWO_4$-MnO_2-NCNO.

Fig. 4. FE-SEM images of the synthesized nanomaterials.

Fig. 5. Experimental Z-scan setup (BS1 & BS2: beam splitter, D1, D2 & D3: detector, S: sample, L1 & L2: lens, AP: aperture)

Fig. 6. OA Z-scan results of (a) MnO_2, (b) $CoWO_4$, (C) NCNO, (d) $CoWO_4$-MnO_2, and (e) $CoWO_4$-MnO_2-NCNO nnocomposites with different incident power. The filled dots are the experimental data and solid lines represent the fitting curves.

Fig. 7. CA Z-scan results of (a) MnO_2, (b) $CoWO_4$, (C) NCNO, (d) $CoWO_4$-MnO_2, and (e) $CoWO_4$-MnO_2-NCNO nanocomposites with different incident power. The filled dots are the experimental data and solid lines represent the fitting curves

Figures

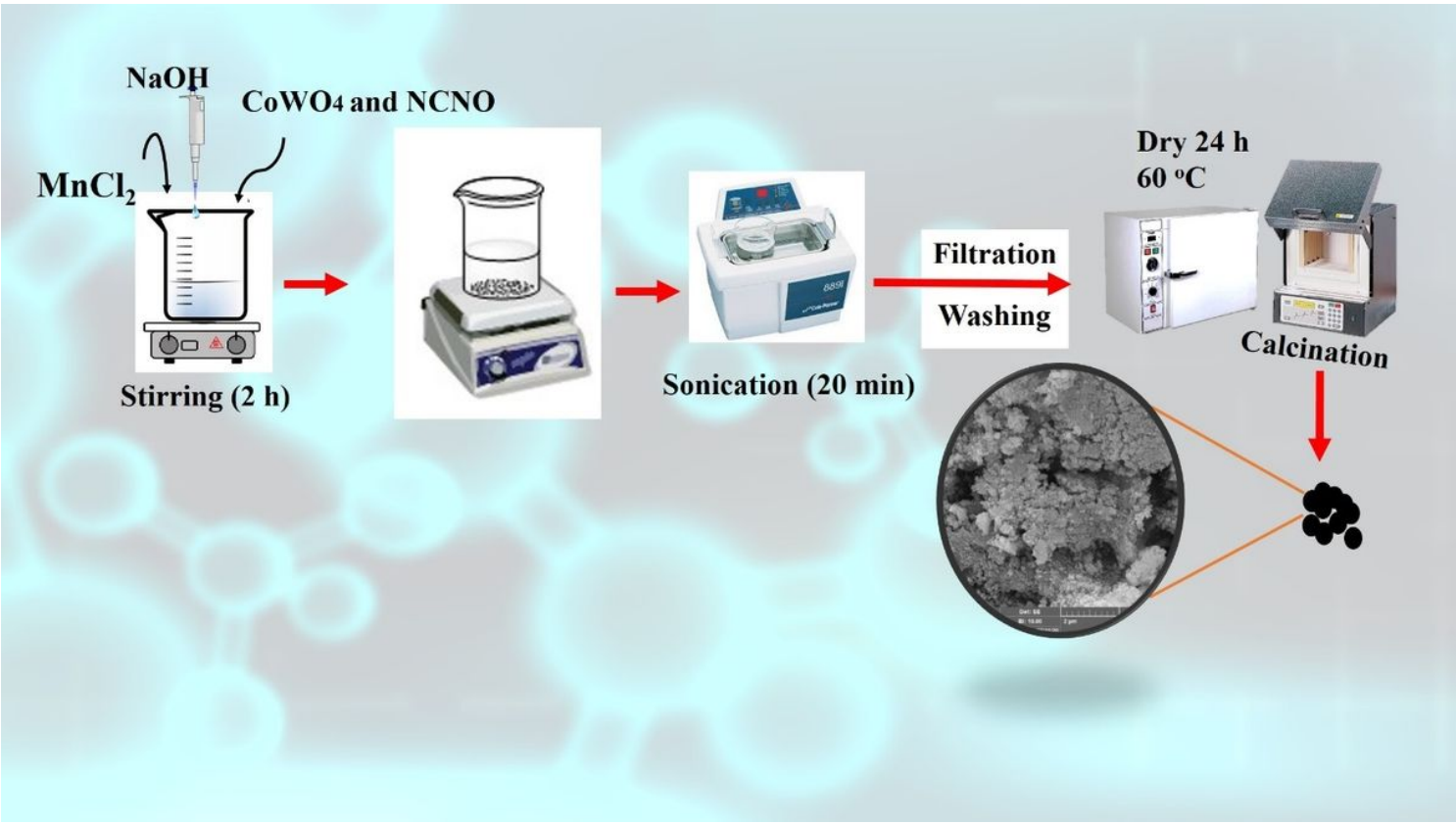

Figure 1

Experimental procedure of synthesized CoWO4-MnO2-NCNO nanocomposites.

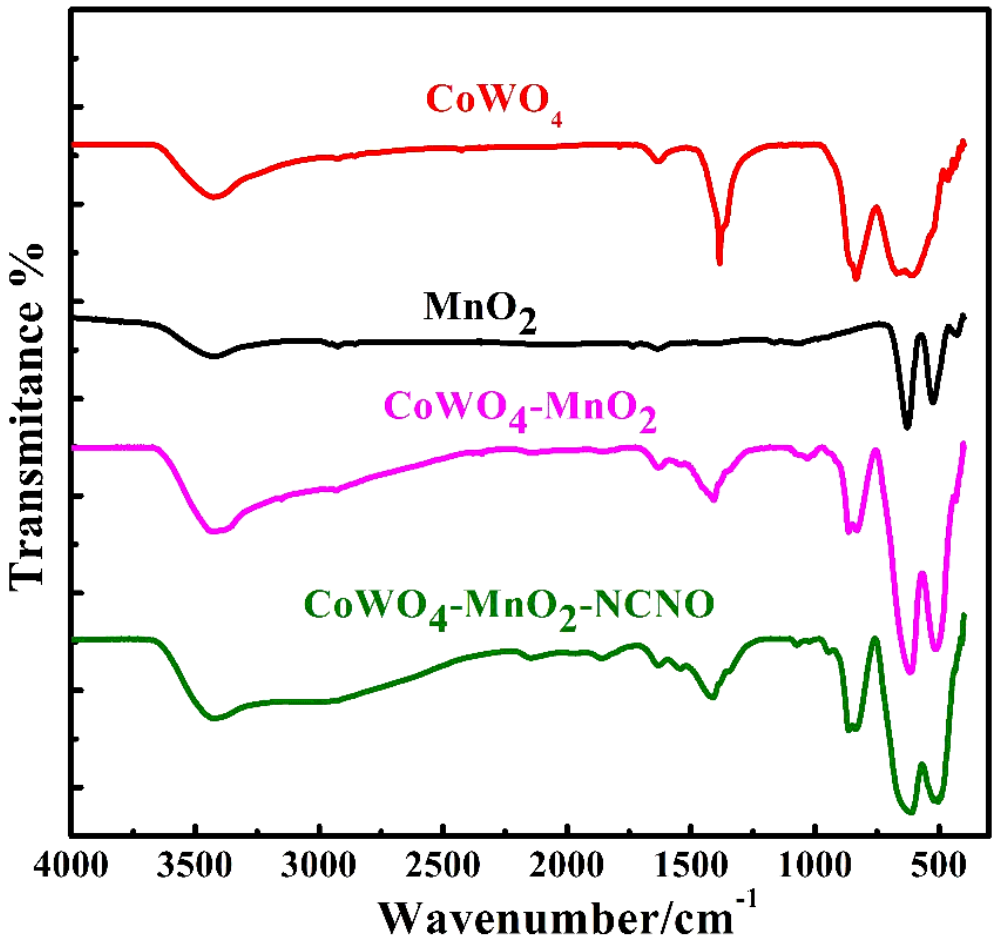

Figure 2

FTIR spectra of the synthesized nanomaterials.

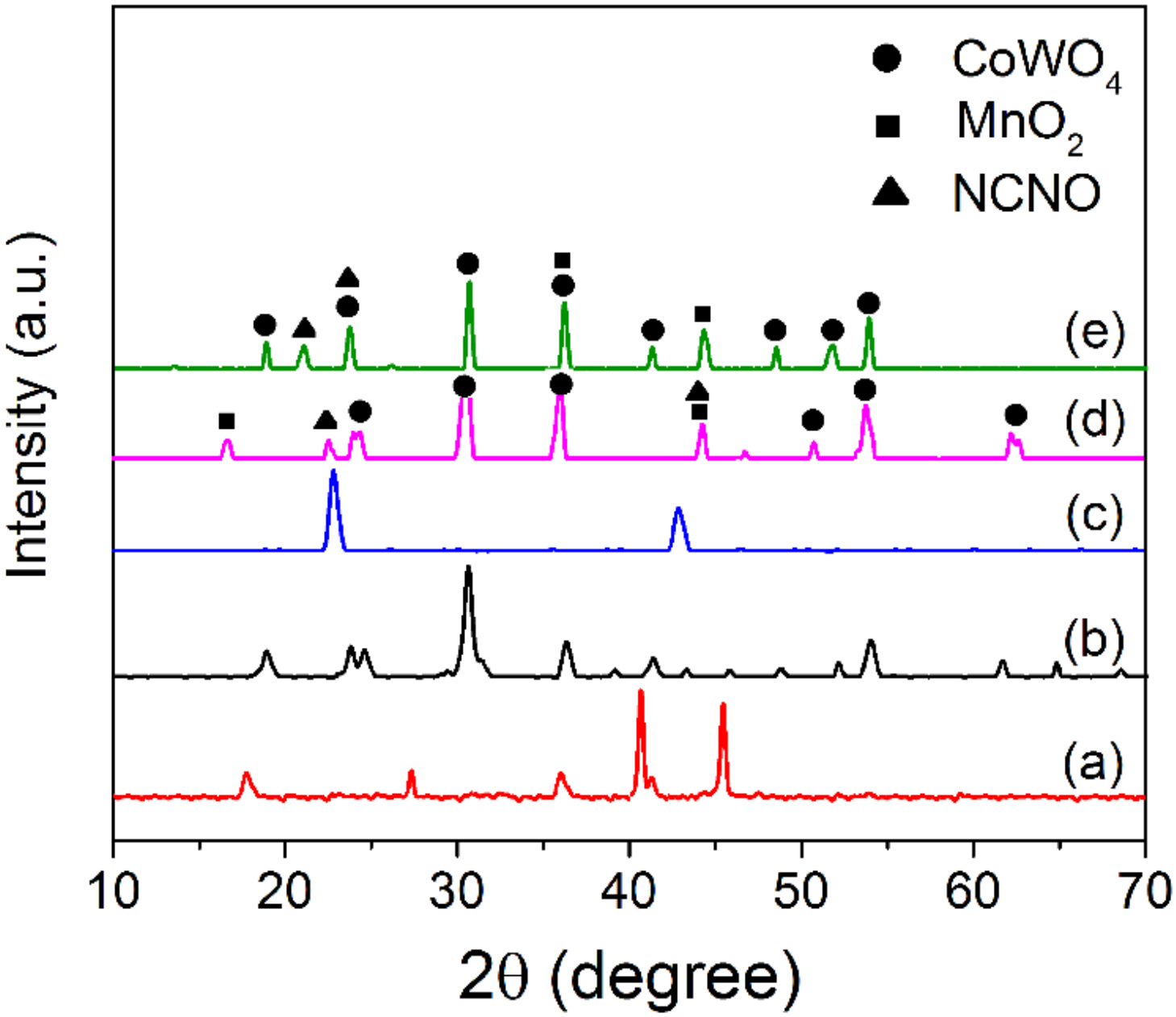

Figure 3

XRD patterns of the (a) MnO2, (b) CoWO4, (c) NCNO, (d) CoWO4-MnO2, and (e) CoWO4-MnO2-NCNO.

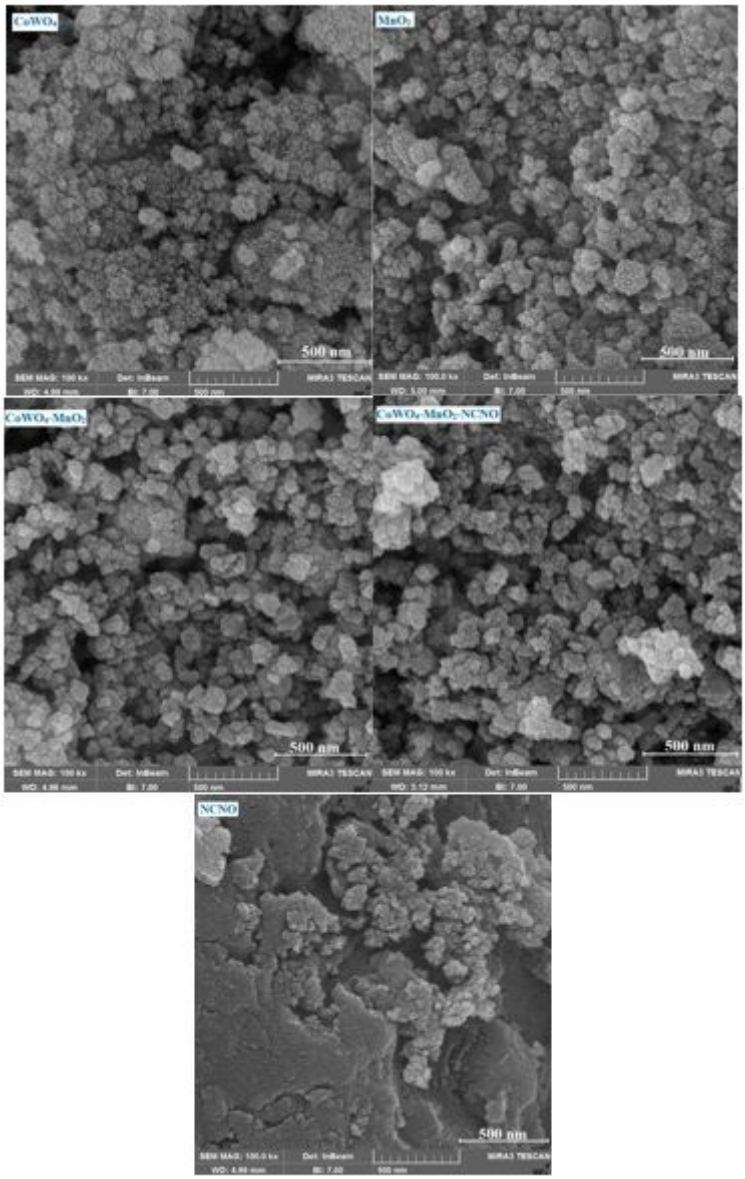

Figure 4

FE-SEM images of the synthesized nanomaterials.

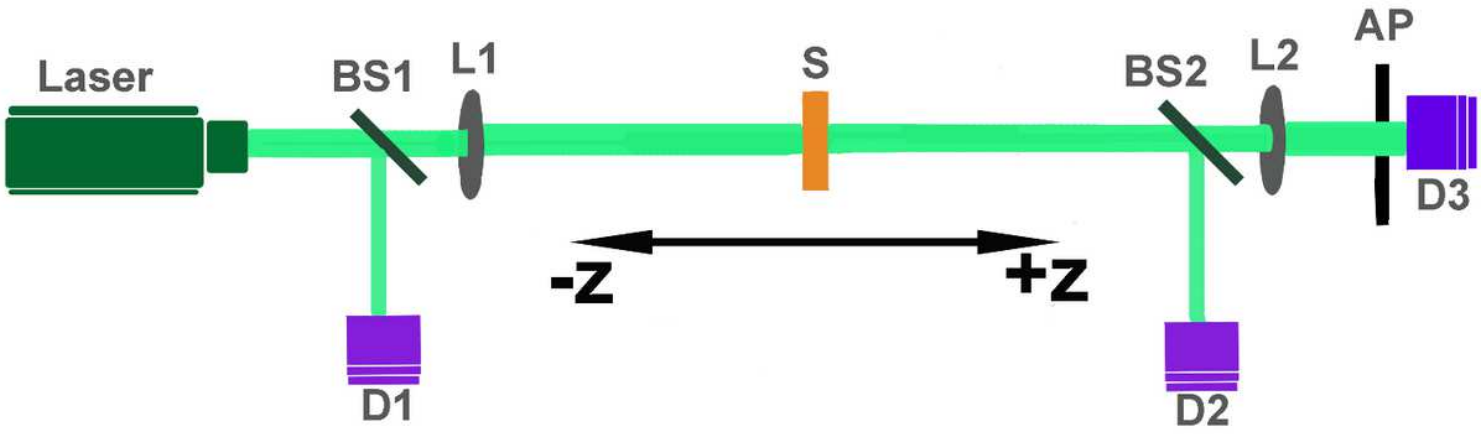

Figure 5

Experimental Z-scan setup (BS1 & BS2: beam splitter, D1, D2 & D3: detector, S: sample, L1 & L2: lens, AP: aperture)

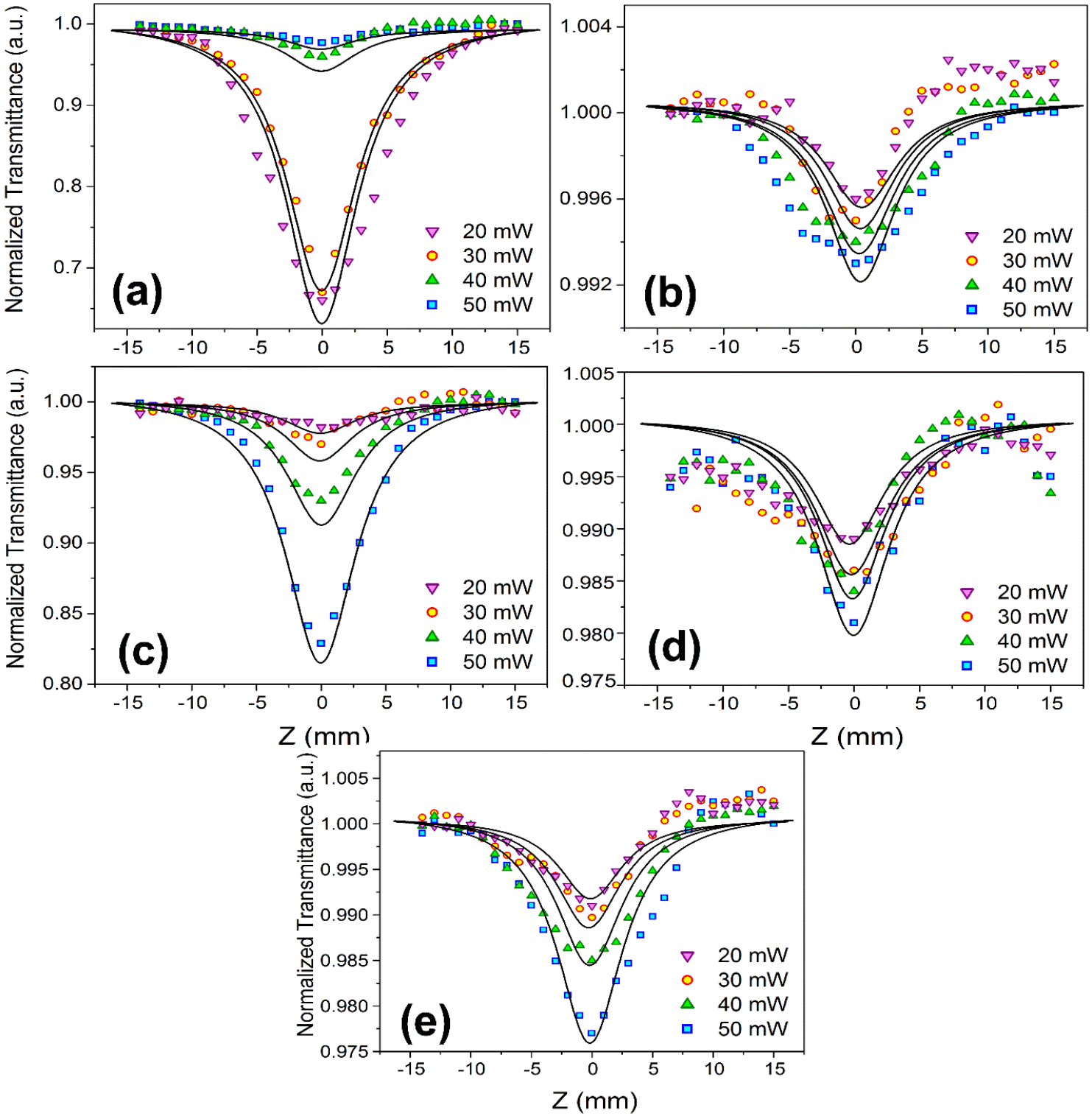

Figure 6

OA Z-scan results of (a) MnO2, (b) CoWO4, (C) NCNO, (d) CoWO4-MnO2, and (e) CoWO4-MnO2-NCNO nnocomposites with different incident power. The filled dots are the experimental data and solid lines represent the fitting curves.

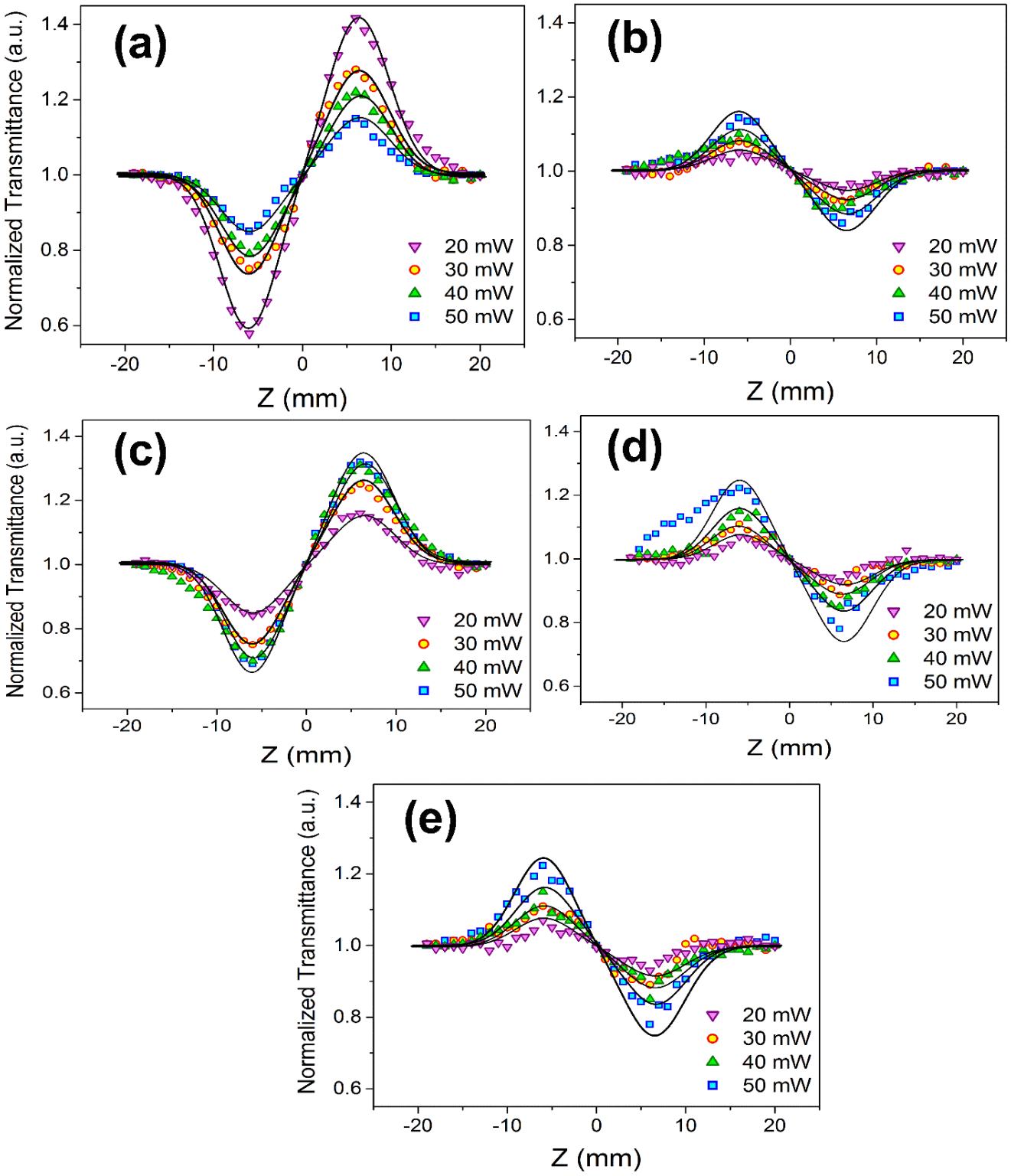

Figure 7

CA Z-scan results of (a) MnO2, (b) CoWO4, (C) NCNO, (d) CoWO4-MnO2, and (e) CoWO4-MnO2-NCNO nanocomposites with different incident power. The filled dots are the experimental data and solid lines represent the fitting curves